NAVAL POSTGRADUATE SCHOOL

MONTEREY, CALIFORNIA

THESIS

A TEMPORAL AND SPATIAL ANALYSIS OF WAVE–GENERATED FOAM PATTERNS IN THE SURF ZONE

by

Charlotte A. Benbow

December 2015

Thesis Advisor:	Jamie MacMahan
Second Reader:	Edward Thornton

Approved for public release; distribution is unlimited

THIS PAGE INTENTIONALLY LEFT BLANK

1. AGENCY USE ONLY *(Leave blank)*	**2. REPORT DATE** December 2015	**3. REPORT TYPE AND DATES COVERED** Master's thesis	
4. TITLE AND SUBTITLE A TEMPORAL AND SPATIAL ANALYSIS OF WAVE–GENERATED FOAM PATTERNS IN THE SURF ZONE		**5. FUNDING NUMBERS**	
6. AUTHOR(S) Charlotte A. Benbow			
7. PERFORMING ORGANIZATION NAME(S) AND ADDRESS(ES) Naval Postgraduate School Monterey, CA 93943-5000		**8. PERFORMING ORGANIZATION REPORT NUMBER**	
9. SPONSORING /MONITORING AGENCY NAME(S) AND ADDRESS(ES) N/A		**10. SPONSORING / MONITORING AGENCY REPORT NUMBER**	
11. SUPPLEMENTARY NOTES The views expressed in this thesis are those of the author and do not reflect the official policy or position of the Department of Defense or the U.S. Government. IRB Protocol number ____N/A____.			
12a. DISTRIBUTION / AVAILABILITY STATEMENT Approved for public release; distribution is unlimited		**12b. DISTRIBUTION CODE**	

13. ABSTRACT (maximum 200 words)

Aerial videos of the surf zone at Sand City, Monterey Bay, CA, were acquired using an unmanned aerial vehicle. Videos of 26 individual bores were converted to still images and were georectified, georeferenced, and post processed. The size, shape, and evolution of the wave generated foam patterns within the surf zone were analyzed. The results were tested against two existing hypotheses of foam pattern generation, Obliquely Descending Eddies (ODEs) and self-organization due to bubble rise. Three foam regions within the surf zone were recognized. The largest region, the foam mat, encompasses nearly the entire surf zone and is described as a mat of foam that develops obvious foam holes. The areas of the holes grew in area and elongated with time. The results were inconsistent with the two theories of foam hole generation. The fringe region is the most seaward foam region and is marked with circular foam rings that become larger in area and more distinct with time. The fringe region data are contrary to observations of ODEs but is consistent with the theory of self-organization due to bubble rise. The gap region, located between the plunge point and the splash up created by the bore collapse, is marked by horizontal foam tubes oriented in the cross-shore direction. The foam tubes are likely created in the convergent region between two counter-rotating vortices.

14. SUBJECT TERMS Wave Breaking, Foam, Obliquely Descending Eddies, Aerial Imagery, Image Processing			**15. NUMBER OF PAGES** 57
			16. PRICE CODE
17. SECURITY CLASSIFICATION OF REPORT Unclassified	**18. SECURITY CLASSIFICATION OF THIS PAGE** Unclassified	**19. SECURITY CLASSIFICATION OF ABSTRACT** Unclassified	**20. LIMITATION OF ABSTRACT** UU

THIS PAGE INTENTIONALLY LEFT BLANK

A TEMPORAL AND SPATIAL ANALYSIS OF WAVE–GENERATED FOAM PATTERNS IN THE SURF ZONE

Charlotte A. Benbow
Lieutenant, United States Navy
B.S., United States Naval Academy, 2008

Submitted in partial fulfillment of the
requirements for the degree of

MASTER OF SCIENCE IN PHYSICAL OCEANOGRAPHY

from the

**NAVAL POSTGRADUATE SCHOOL
December 2015**

Approved by: Jamie MacMahan
                 Thesis Advisor

                 Edward Thornton
                 Second Reader

                 Peter Chu
                 Chair, Department of Oceanography

THIS PAGE INTENTIONALLY LEFT BLANK

ABSTRACT

Aerial videos of the surf zone at Sand City, Monterey Bay, CA, were acquired using an unmanned aerial vehicle. Videos of 26 individual bores were converted to still images and were georectified, georeferenced, and post processed. The size, shape, and evolution of the wave generated foam patterns within the surf zone were analyzed. The results were tested against two existing hypotheses of foam pattern generation, Obliquely Descending Eddies (ODEs) and self-organization due to bubble rise. Three foam regions within the surf zone were recognized. The largest region, the foam mat, encompasses nearly the entire surf zone and is described as a mat of foam that develops obvious foam holes. The areas of the holes grew in area and elongated with time. The results were inconsistent with the two theories of foam hole generation. The fringe region is the most seaward foam region and is marked with circular foam rings that become larger in area and more distinct with time. The fringe region data are contrary to observations of ODEs but is consistent with the theory of self-organization due to bubble rise. The gap region, located between the plunge point and the splash up created by the bore collapse, is marked by horizontal foam tubes oriented in the cross-shore direction. The foam tubes are likely created in the convergent region between two counter-rotating vortices.

THIS PAGE INTENTIONALLY LEFT BLANK

TABLE OF CONTENTS

THIS PAGE INTENTIONALLY LEFT BLANK

LIST OF FIGURES

THIS PAGE INTENTIONALLY LEFT BLANK

ACKNOWLEDGMENTS

First and foremost, I would like to thank my advisors, Jamie MacMahan and Ed Thornton. Without their time, energy, creativity, patience and support this thesis would have been impossible. To Mike Cook and Keith Wyckoff thank you for all your help, encouragement and ingenious engineering both in the field and in the computer lab. To the University of Miami, thank you for providing the UAV equipment. To my classmates, thank you for keeping spirits high in the tough times, and for always lending a helping hand. And lastly to Professor Mary Batteen, thank you for instilling in all of us a love of learning and a passion for the oceans.

THIS PAGE INTENTIONALLY LEFT BLANK

I.   INTRODUCTION

As waves break near the shore, processes occur that trap air below the ocean surface creating bubbles (Thorpe et al. 1999). The size of the bubble determines how fast it will rise to the surface, with the larger bubbles rising fastest. Some of the bubbles break as soon as they reach the surface; others remain on or just below the surface, creating patches of foam. Directly in front of, above, and behind the wave crest, the foam exists as a dense mat with few gaps or holes. Thorpe et al. (1999) noted that due to the nature of the turbulent processes in the surf zone, the foam left behind as the bore progresses toward the beach morphs into coherent patterns, recognizable to the naked eye.

Waves break near the shore due to kinematic and dynamic instabilities (Thornton 1979). If the water at the crest of the wave moves faster than the wave itself, the wave will collapse and break; this is the *kinematic instability*. The *dynamic instability* develops when the change in the vertical velocity at the sea surface exceeds gravity. When the *dynamic instability* occurs, the wave becomes too steep (the ratio of the deep-water wave height to the wavelength is greater than 1/7), and the wave becomes unstable and breaks. The surf similarity parameter, ξ_b, is widely used as a guide for determining the different types of breaking that occur (Battjes 1974). The surf similarity parameter is controlled by beach slope angle, breaker height and deep-water wavelength. There are three types of breaking waves: spilling ($\xi_b<0.4$), plunging ($0.4<\xi_b<2$), and surging ($\xi_b>2$). Determining the breaker type is important because the type defines how the bubbles and foam are generated as the wave breaks.

Longuet-Higgins and Turner (1974), describe how a spilling breaker generates foam, using the "entraining plume" model. According to their model, a spilling breaker will break gently at the crest of the wave, trapping air. The air-water mixture will stay at the surface because the foamy, air-water mixture is less dense than the water surrounding it. The foam patch will begin to grow and ride down the front of the spilling breaker due to gravity. More air is entrained into the foam patch along the front edge as the patch rides down the wave, while more water is entrained into the foam patch from below, along the foam-water interface. The foam damps the growth of the crest, and when the

damping process exceeds the shoaling process, the crest of the spilling breaker rounds and the foam patch slides backward over the crest. Turner and Turner (2011) also discuss how foam is generated behind a spilling breaker. Their theory originates with the "entraining plume" model, but they add that foam generated in front of the crest can be entrained downward and will pass under the crest. Because the foam is less dense and more buoyant than the surrounding water, it will float to the surface and will join up with the foam that passed over the crest. This foam patch remains behind as the bore continues to progress toward the shore.

As opposed to the gentle breaking process of a spilling breaker, a plunging breaker becomes vertical and then overturns, breaking kinematically and throwing a jet of water forward of the wave (Peregrine 1983). Derakhti and Kirby (2014) outlined three air entrainment mechanisms for plunging breakers. First, as the jet crashes back to the surface, the tube closes and entrains air, creating bubbles and foam. Then, as the jet crashes into the surface, splashes are sent up forward of the bore. As the bore collapses, a cloud of bubbles and water are thrown skyward. As this secondary splash falls back to the surface, even more air is entrained in the water, and more bubbles and foam are produced. This process of jet formation and splash down can be repeated several times as the wave moves toward the shore. Once the wave becomes a bore, more air is entrained in a process similar to that described above for a spilling breaker.

Turbulent processes in the wave-breaking region are not well understood. In the past, hot-film and laser-Doppler anemometers were used to measure turbulence in the surf zone; however, these point measurements were not sufficient to describe the 3-dimensional aspects of turbulence (Ting and Reimnitz 2015). Foam and bubbles in the surf zone can cause signal dropout, further complicating efforts to capture information on turbulent processes (Nadaoka et al. 1989). In recent years, particle image velocimetry (PIV) and volumetric three-component velocimetry (V3V) have been used to measure breaking wave generated turbulence in laboratory wave tanks (Ting and Nelson 2011, Ting 2013, Ting and Reimnitz 2015). However, these techniques have yet to be adapted to field measurements. Nadaoka and Kondoh (1982) observed that the intensity of turbulence at the bottom of the water column is correlated with the turbulence at the top

of the water column. Therefore, the foam on the surface can be used as a tracer to describe total water column turbulence. These turbulent properties are important to categorize because they drive processes like sediment transport, water clarity, and the transport of pollutants in the surf zone. The presence of foam affects the ability to see through the water column as well as the performance of acoustic and optical sensors. Understanding how the foam evolves will help the operator better exploit the environment.

Thorpe et al. (1999) and Thorpe (2007) describe two mechanisms for generating foam holes in the surf zone; obliquely descending eddies (ODEs)/hairpin vortices, and self-organization by rising bubbles. In a wave tank, Nadaoka et al. (1989) observed that in the wave breaking region two types of eddies develop, namely horizontal eddies and ODEs. The horizontal eddies, which are located around the wave crest, have a horizontal axis aligned parallel to the wave crest. The ODEs form behind the wave crest and in the region between two horizontal eddies. These ODEs (Figure 1) have an axis that is aligned perpendicular to the wave crest and tilted downward in the offshore direction (Nadaoka et al. 1989). Nadaoka et al. (1989) also observed that the ODEs can reach the bottom and are a mechanism for suspending sediment in the water column. As the eddy reaches the bottom and "kicks up" sediment into the water column the buoyancy of the bubbles in the eddy help to further move the sediment upward in the water column. Hairpin vortices, also known as reversed horseshoe vortices, have a similar structure to ODEs. The legs of the hairpin vortices are made up of two counter-rotating ODEs connected at the base by a transverse vortex (Watanabe et al. 2005, Farahani and Dalrymple 2014, Ting and Reimnitz 2015).

Figure 1.   Schematic of Eddies in the Wave Breaking Region
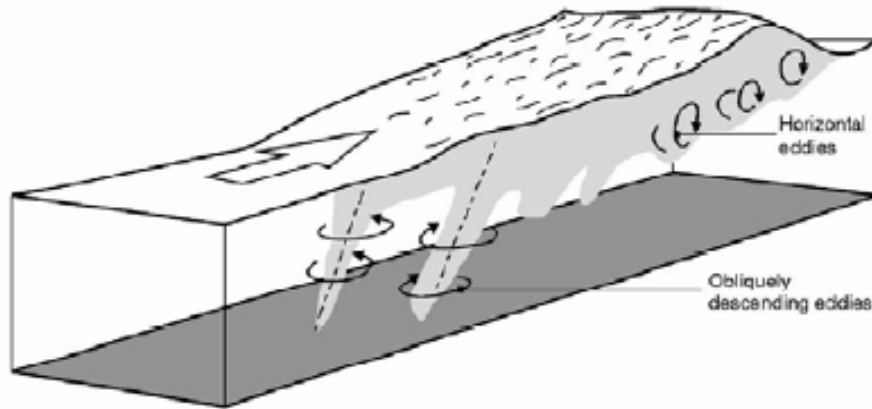
Horizontal eddies depicted under the breaking wave and alligned parallel to the wave crest. Obliquely descending eddies depicted behind the wave, extending from the surface to the sea bed. Arrow depicts direction of wave propogation. Source: Nadaoka K., Hino M.,Koyano Y., 1989, Structure of the turbulent flow field under breaking waves in the surf zone, *J. Fluid Mech.*, 204, 359–387.

The second possible mechanism for foam hole generation is the process of self-organization by rising bubbles. Derakhti and Kirby (2014) showed by numerical model that in both spilling and plunging breakers the drag force between the bubbles and the liquid surrounding the bubbles was the primary mechanism for momentum exchange in the vertical direction. Therefore, as the larger bubbles rise rapidly to the surface they impart upward momentum on the water surrounding them (Thorpe et al. 1999). When the larger bubbles reach the surface, the upward-induced motion continues briefly, causing divergence at the surface and a flow of smaller bubbles radially outward, creating a region of no foam or bubbles. They also noted that there is a downward motion (due to continuity) that occurs at a greater radial distance.

The primary goal of this thesis is to study the nearly circular patches of foam and foam holes that emerge behind bores inside the surf zone. The foam rings that exist between the foam mat and the open water will also be studied along with the foam tubes that develop between the plunge point and the secondary splash point. The spatial and temporal scales of these foam patterns have not been quantified. With the advances made in small, inexpensive, unmanned aerial vehicles, persistent overhead imaging of the

natural surf zone is now possible. Aerial imagery of the surf zone is analyzed to determine how the shape and size of the foam holes evolve with time. These foam patches are used as a passive tracer to describe the turbulent processes that occur due to wave breaking, and the statistics collected from analyzing these foam patches are used to quantitatively describe the turbulence.

THIS PAGE INTENTIONALLY LEFT BLANK

II. METHODOLOGY

A. EQUIPMENT AND EXPERIMENT DESIGN

The DJI Phantom 2 Vision+ (hereafter referred to as the Phantom 2) quadcopter, unmanned aerial vehicle, UAV (see Figure 2) was used to acquire aerial imagery of the surf-zone. The lightweight, quad rotor, battery powered aircraft was chosen for this project because of its ease of flight, image capabilities owing to its ability to hover in a station-keeping mode, and relatively low cost ($1k). The Phantom 2 has approximately 20-minute flight time. The Phantom 2 supports a gimbaled, fish-eye lens camera located on the underside of the vehicle. The camera can record high definition video at 1080p30, 1080 horizontal lines of vertical resolution, progressive scan, where every horizontal line is drawn in sequence and an image capture rate of 30 frames per second. The camera can also continuously record still images at a resolution of 4384×3288 pixels at 1 frame every 3 seconds. Video mode rather than still image mode was chosen to maximize the frequency at which images were collected. The user can choose between either 85° or 110° recording field of view angles (http://www.dji.com/product/phantom-2-vision-plus/spec). Based on camera specifications, the field of view and resolution in pixel/meter were calculated for various flight altitudes assuming the UAV was directly above the surf zone (Figure 3). The FAA maximum flight altitude for unmanned aerial systems is 152.4 m (shown as horizontal black line in Figures 3c and 3d) [http://www.faa.gov/news/press_releases/news_story.cfm?newsId=18295]. The field of view was decreased by 20% to account for the portion of the image that is lost during image processing (image processing is discussed in greater detail below). Based on these calculated values, a flight altitude between 76 and 91 meters was chosen to observe the estimated width of the surf zone O(100m), conform to FAA regulations on UAVs and to resolve the features of interest. It is desirable to acquire aerial imagery from directly above the surf zone with no tilt to the camera to minimize image distortion. However, in order to capture the entire width of the surf zone (approximately 100 meters) at a high enough resolution and capture all of the ground control points (GCPs), some of which were located on the beach, it was necessary to apply a slight tilt to the camera. The

wireless connection between the quadcopter and the remote control also limited the maximum flight altitude due to signal drop out at altitudes above approximately 100 meters. The calculations of pixel resolution determined the size of the GCPs required to attain sub-pixel accuracy.

Figure 2.   DJI Phantom 2 Vision+

The DJI Phantom 2 Vision+ Quadcopter used during this experiment equipped with a small 14 megapixel gimbaled camera, compass, live video stream downlink. Source: DJI, 2015: DJI Phantom 2 Vision +. Accessed 8 October 2015. [Available online at http://www.dji.com/product/phantom-2-vision-plus/feature.]

Figure 3.   Resolution (pix/m) and Field of View (m) versus Elevation (m)
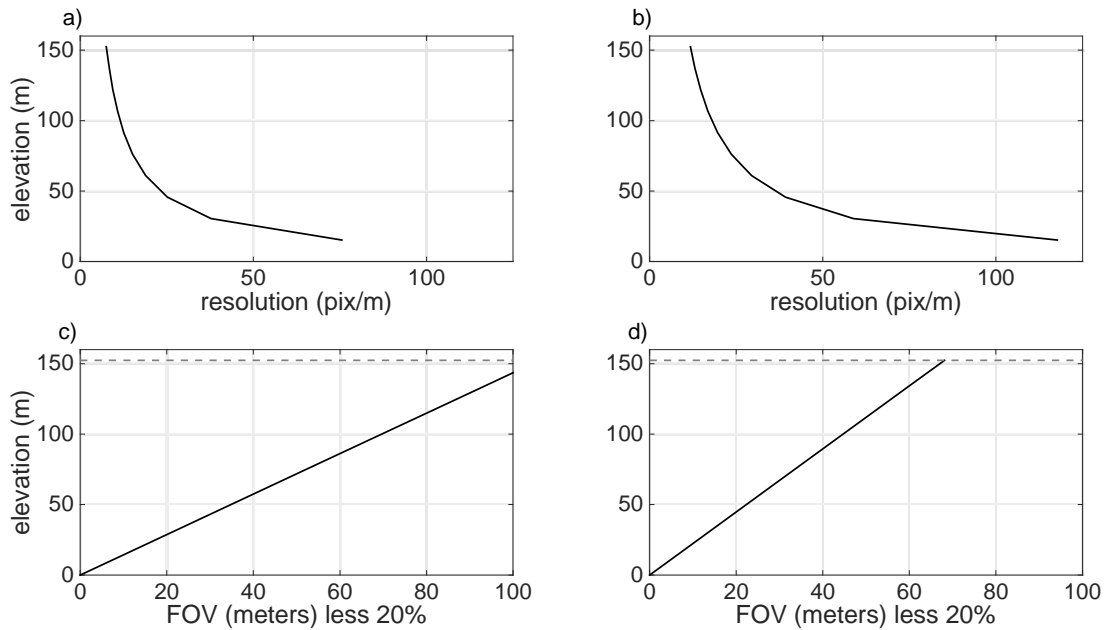
a) resolution versus elevation for a view angle of 110° b) resolution versus elevation for a view angle of 85° c) FOV versus elevation for a view angle of 110° (solid line) FAA Maximum allowed flight altitude (dashed line) d) FOV versus elevation for a view angle of 85° (solid line) FAA Maximum allowed flight altitude (dashed line)

8

Ground control points (GCPs) are needed to georectify and georeference images. For image processing purposes it is desirable to have several pixels fall within the GCP, this is called sub-pixel accuracy. Several 0.61-meter diameter plywood circles were painted neon pink and used as GCPs. The pink color was chosen so that the GCPs would stand out against the wet sand, water, foam and breaking waves. Five of the GCPs were placed atop pipes that were jetted into the sand. One of the pipe GCPs was located within the surf zone and broke in half during active wave breaking and had to be removed. Three other pipe GCPs were located in the swash zone with the last pipe GCP located just above the high water line. Four additional GCPs were placed on the sand just above the high water line and within the field of view (Figure 4).

Figure 4.   Undistorted Image Being Georectified
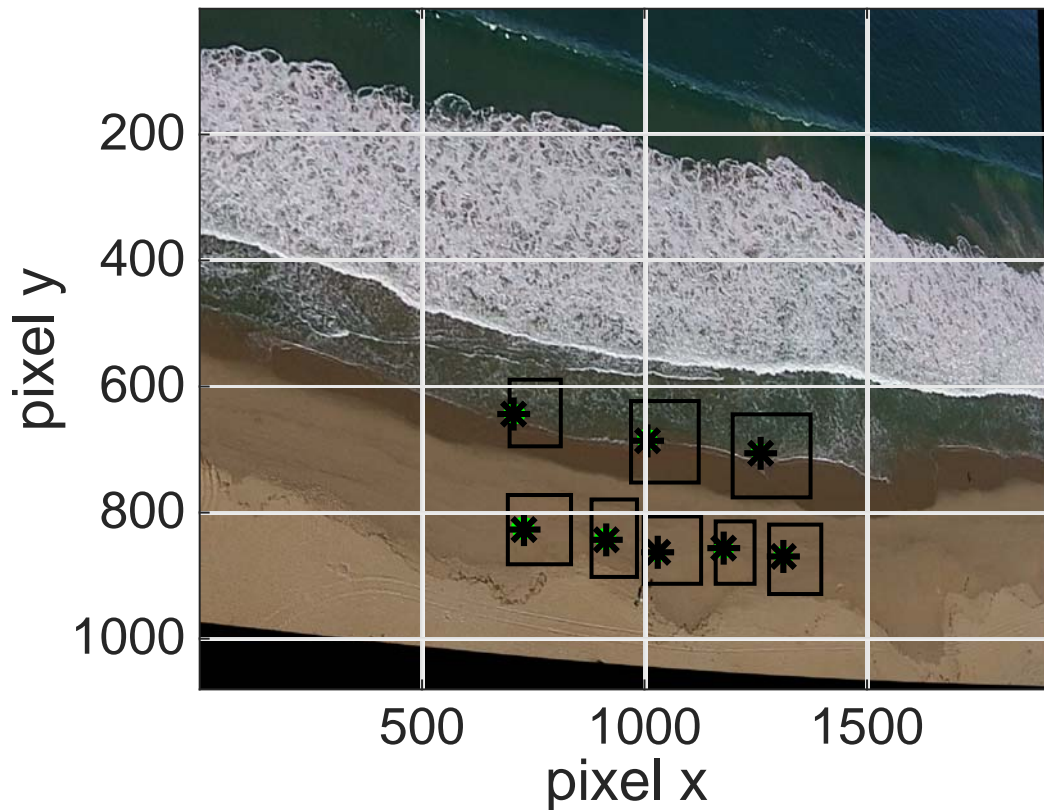
Black boxes indicate search areas, neon green pixels are pixels with color matches to the ground control point, black asterisk is ground control point.

B.   DATA COLLECTION AND PROCESSING

The video of the surfzone foam patterns was obtained on a mostly dissipative beach at Sand City, Monterey Bay, CA on 12 FEB 2015. The beach slope within the surf zone is approximately (1:100) (MacMahan et al. 2005). Due to the location of the headlands and effects from the Monterey Bay Submarine Canyon, waves at Sand City are typically shore normal, resulting in weak alongshore currents and the formation of rip currents (MacMahan et al. 2005). Rip currents were avoided in this study. Wave heights, wave direction and wave frequencies were determined by analyzing sea surface elevation data collected at wave buoy 46042, located just outside of Monterey Bay (Figure 5). The wave height on 12 February was 1.87 meters and the peak period was 13.79 seconds. The swell wave direction is from the west. The day of collection was specifically chosen due to the long wave period and the narrow frequency band of the incoming waves (Figure 5). A longer wave period was desirable because it allows more time for the foam and foam holes to develop, move and change before the next wave broke. The narrow frequency band indicates that the breaking waves are swell waves, and that they are not contaminated with waves of other frequencies. In this data set, the observed waves break initially as plunging breakers, but quickly become spilling breakers and only one jet/splash down cycle is recorded. Eleven videos were collected, with video length limited to less than 2 minutes to make the data size more manageable. Continuous in flight video downlink was enabled through the use of the DJI Phantom cell phone application and the video feed was constantly monitored on a cell phone to ensure that the ground control points were in the center of the field of view. The locations of the GCPs, with horizontal accuracy on the O(cm), were determined by post-processing GPS data from a survey-grade GPS receiver deployed on the center of the GCPs.

Figure 5.   Sea Surface Elevation Spectrum Buoy 46042
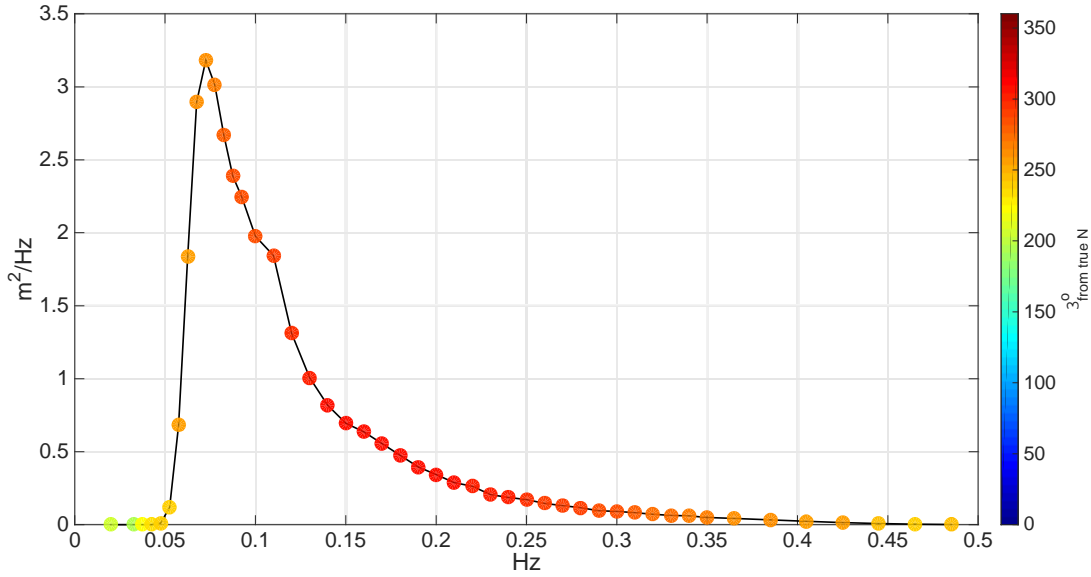
Narrow-band sea surface elevation spectrum at buoy 46042 located just outside Monterey Bay on 12 February. The wave height was 1.87 meters and the peak period was 13.79 seconds. The wave direction for the peak period is from the west.

The video was downloaded and each frame was converted to a still image. Every 10th image was selected, providing 3 frames per second instead of 30. This was done to keep the data size more manageable while keeping the image collection frequency high enough to capture the features of interest. To remove fish eye lens distortion, the camera's intrinsic parameters must be known or calculated. MATLAB provides a simple camera calibration application that determines intrinsic camera parameters using the methods described in Heikkilä and Silvén (1997) and Zhang (2000). These camera parameters are then applied to each image to remove the fish eye distortion.

The undistorted photos were georectified and georeferenced similar to a process described by Brouwer et al. (2015). Georectification is the process of taking a two-dimensional (2D) image and warping it, using a transformation matrix, to match an earth-based three-dimensional (3D) coordinate system. Using a projective transformation matrix, the image pixel containing the ground control point was matched to the latitude and longitude of the ground control point measured in the field. To automate the process, a set of search boxes in the image, each containing a ground control point, were created

(outlined in black in Figure 4). It is necessary to use a search box because the UAV moves slightly with wind gusts. Each pixel within each search box was then evaluated to determine if the pixel's red-green-blue color value fell within a range of values matching that of the pink ground control point (all matching pixels displayed in green in Figure 4). The center of mass of each set of matching pixels was calculated and that pixel was then stored as the image pixel location corresponding to a ground control point (shown as a black asterisk in Figure 4). The process of georectification was essential because knowing the size of each pixel was required in order to determine the size of the foam and foam holes. Georeferencing allows the user to spatially compare georectified images between frames. Each pixel in an image is assigned a corresponding x and y reference value, thus enabling the conversion from pixel space to latitude and longitude space. Once the images were undistorted, georectified and georeferenced, they were rotated so that the bore would be parallel to the x-axis (Figure 6). This was done so that the analysis is described in cross-shore and along-shore directions relative to the bore.

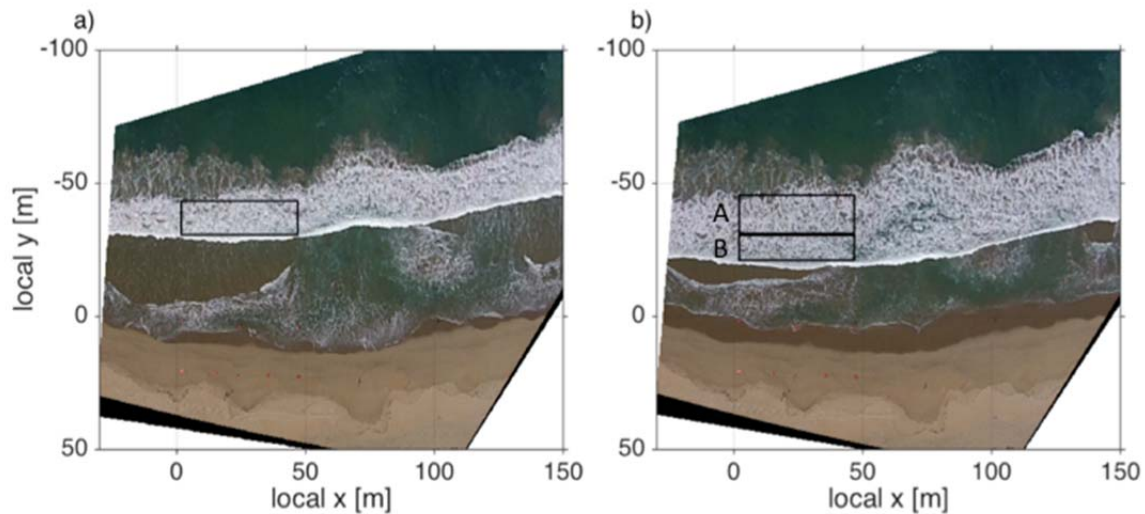Figure 6.   Georeferenced, Georectified and Rotated Image
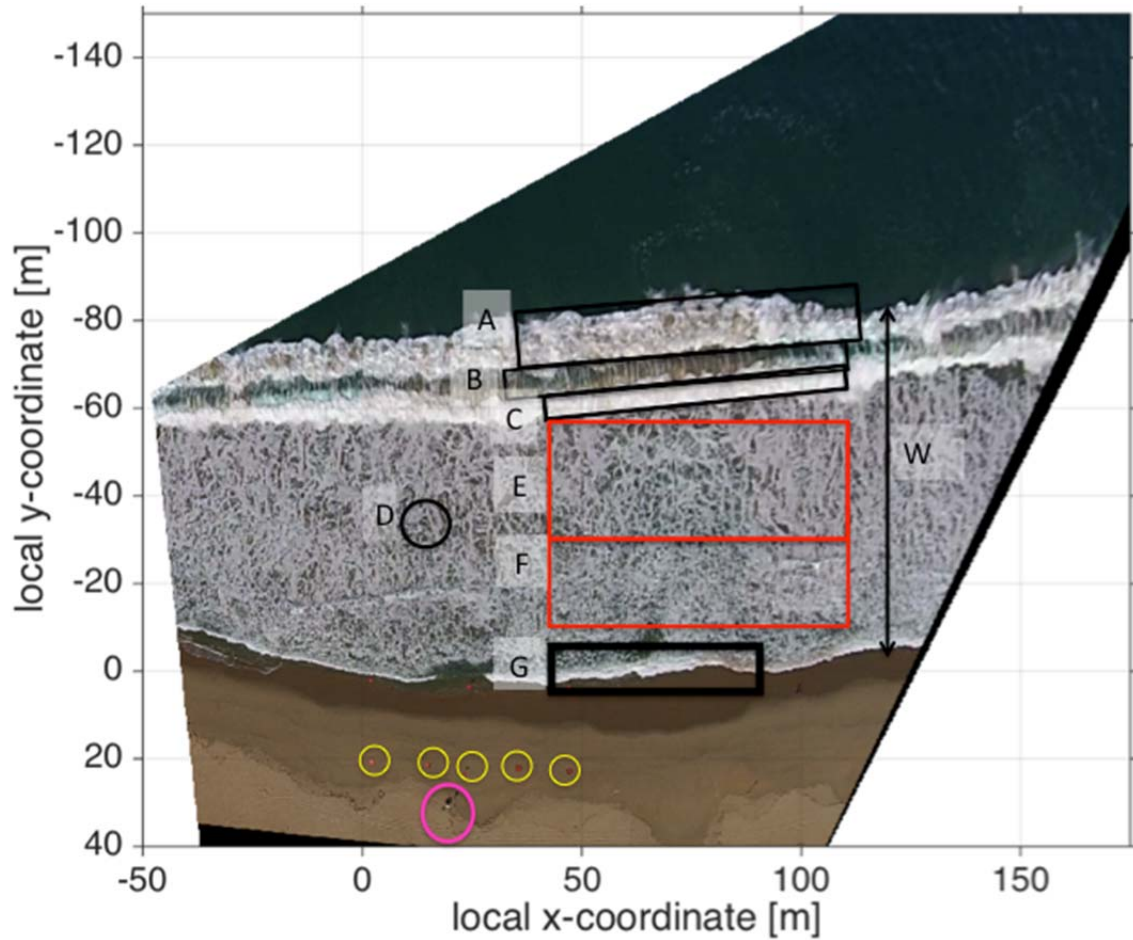
Rectangle A depicts the fringe region, rectange B depicts the gap region, rectangle C is the plunging breaker, circle D represents a foam hole, rectangle E depict a top box, rectangle F depicts a bottom box, rectangle G depicts a self similar bore, W depicts the width of the surfzone. The yellow circles indicate the GCPs and the pink circle shows the UAV operator.

The undistorted, rectified, referenced and rotated images were then individually analyzed and only a small portion of each image, the part filled with foam and holes, was saved for further analyses. As a wave broke, the area just behind the wave was selected as the first top box (Figure 7a). The left and right bounds of the box were selected so that any wave reflections from the shoreline or rip currents in the image would not be included in the sub-box. As the bore progressed toward the shore in each subsequent image, the selected box became larger in the cross-shore, extending from either the edge

of the foam or the front of the next bore on the seaward side to the back edge of the bore on the shoreward side.

As the bore progressed toward the shore there was a point where the foam holes developed two distinct regimes (Figure 6 box E and F and Figure 7b). The more seaward holes had grown and were now significantly larger than the "new" more shoreward holes. At this point the box was split into two boxes depending on the size of the holes. The top box is located between either the front edge of the next bore and the top of the bottom box (Figure 6 box E) or between the seaward side of the foam and the top of the bottom box (Figure 7b box A). The bottom box was located further shoreward, between the bottom of the top box and the backside of the bore (Figure 6 box F and Figure 7b box B). The top and bottom boxes were allowed to grow and change as the bore progressed toward the shore and represent different depths. As a new wave broke the process of analyzing the image and selecting sub-boxes started all over again. Twenty-six individual bores and their associated top and bottom sub-boxes were stored for further analysis.

Figure 7.   Selection of Top and Bottom Sub Boxes

Georectified, georeferenced and rotated image depicting a top and bottom sub-box

14

These subset images were then converted to gray scale images, pixel value between 0 and 1, and then into binary images, pixel value of either 0 or 1. To convert the images into binary images a threshold value had to be determined a priori. Any pixel that had an intensity value larger than the threshold value was converted to a 1 (white) and any pixel that had an intensity value less than the threshold value was converted to a 0 (black). Initially a 0.5 threshold value was applied to all the images. However, after close inspection, it was found that using only one threshold value for all the images did not appropriately classify the holes and foam, and some of the important data were lost. To account for changes in image intensity over a set of images, Carini et al. (2015) and Podobna et al. (2010) created histograms of image intensity to determine the appropriate threshold value to use for each image. In a manner similar to this approach, the mean intensity value of each image was calculated and used as the threshold value. Again, this mean value method was not sufficient to appropriately represent foam and hole. Therefore, a manual approach was adopted.

To manually determine the threshold value, an interactive selection technique (Grande 2000) was performed. For each second (every third image), a subset gray-scale image (Figure 8a) from the longest dataset of top boxes was displayed on the screen along with five binary images, each with a different threshold value (Figure 8). In this example, the image displayed is 13 seconds after wave breaking, and the threshold values displayed on the image are; 0.475, 0.45, 0.425, 0.4 and 0.375 (Figure 8). If the threshold value is set too high, gray pixels that should be turned white are turned black, which causes several holes to become connected and appear much larger than they actually are. If the threshold value is set too low, the gray pixels that should connect to other gray pixel and form a hole turn white, making the holes appear much smaller than they actually are. The threshold value that best represented the foam and holes was recorded. In this case the threshold value selected was 0.475 (Figure 8b). When viewed on a computer screen, it is much easier to differentiate between the different threshold values and their impact on the image. A third-degree polynomial was fit to the threshold values for all times using the longest bore record (Figure 9 grey line) and was then applied to all the bores. The threshold determination was similarly estimated on the longest dataset of

15

the bottom boxes and another third-degree polynomial equation of threshold values was recorded (Figure 9 black dashed line). Note that the threshold values were different between the bottom and top boxes. These threshold values were then used to convert the gray-scale images into binary images for further analysis. The black regions in the binary image correspond to the foam holes and the white regions correspond to the foam.

Figure 8.   Determining the Threshold Value
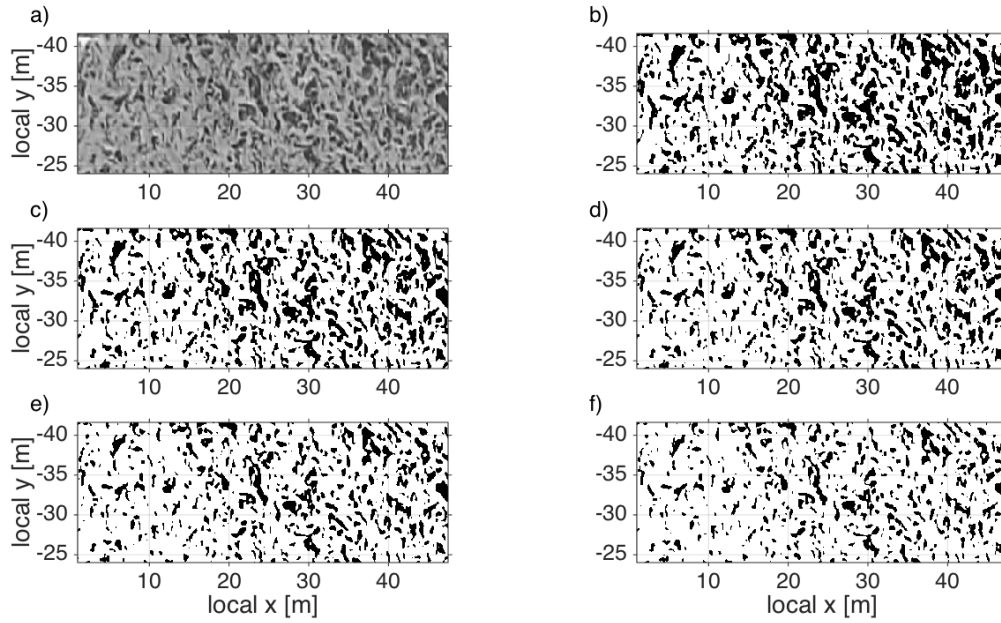
a) gray-scale subset image b) binary image with threshold=0.475 c) binary image with threshold=0.45 d) binary image with threshold =0.425 e) binary image with threshold =0.4 f) binary image with threshold =0.375

Figure 9.   Third-Degree Polynomial of Threshold Values
for Top and Bottom Boxes
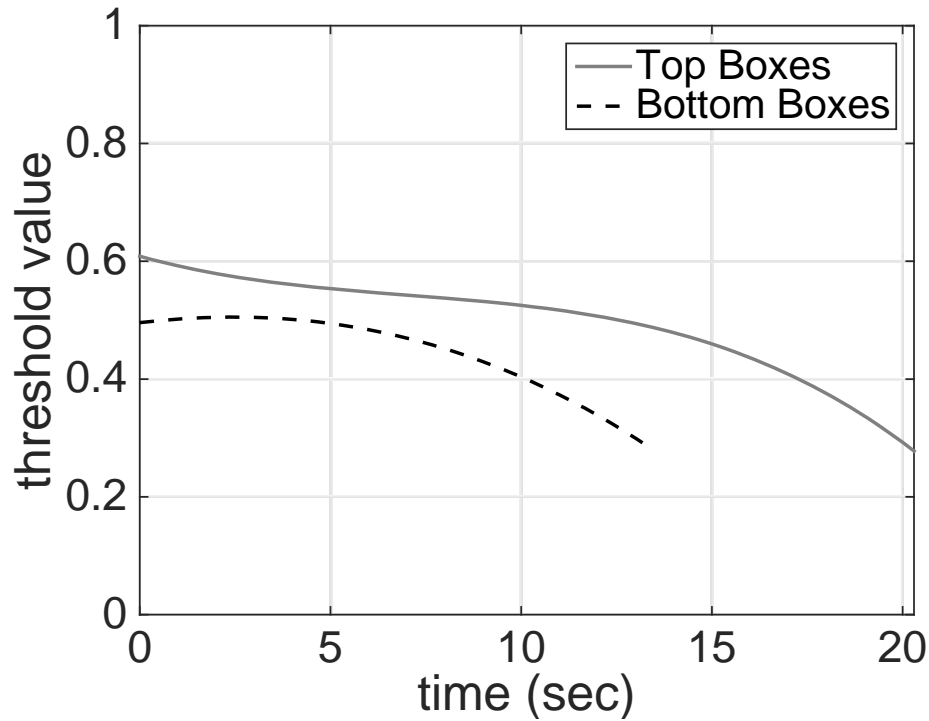
Time series of threshold values for determining whether a pixel should be a 0 or a 1 based on the interactive selection technique and a third-degree polynomial best-fit line. Gray solid line is used for the top boxes and the black dashed line is used for the bottom boxes.

The boundaries between the black regions and white regions were determined and used to calculate the area of the foam holes. While conducting a quality check of the data, it became apparent that some of the regions that were identified as foam holes were in fact small unimportant features within the image, artifacts of the conversion to a binary image. A minimum area was determined that removed the unimportant features while maintaining the features of interest. To determine this minimum area, four of the same binary images were displayed with the boundary between the black and white pixels displayed in red and green (Figure 10). The red boundaries show the areas that are smaller than the assigned cutoff area and the green boundaries show the areas that are larger than the assigned cutoff area. By using this technique, a cutoff area of $0.35m^2$ was chosen and any black region with an area less than this cutoff was disregarded and

17

removed from further analysis. The foam holes that are not outlined by anything are connected to the border and are also removed from further analysis.

Figure 10.   Determining the Minimum Allowable Area
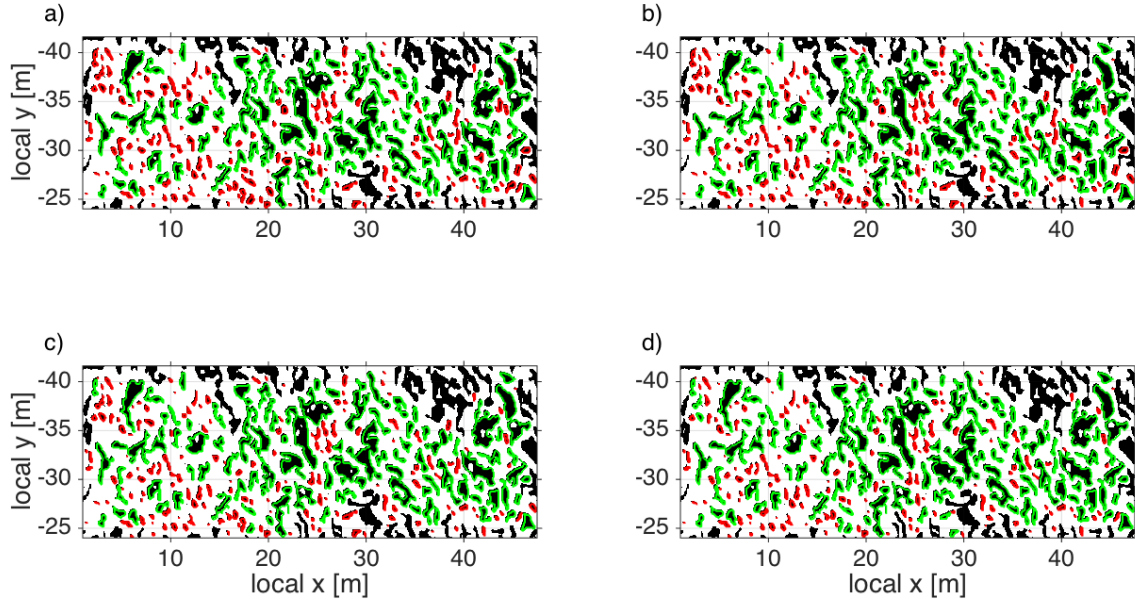
Features included in green, features ignored in red a) cutoff area = 0.4m^2 b) cutoff area = 0.35m^2 c) cutoff area = 0.3m^2 d) cutoff area = 0.25m^2. Features not surrounded by a color are connected to the border and are ignored.

To determine how the foam holes changed with time, various shape factors were analyzed. Shape factors are non-dimensional quantities calculated from the dimensions of the shape, which describe the shape of an object relative to another standard object (Wojnar 2000). The shape factors used in this analysis are elongation, circularity, and compactness. Elongation, defined as,

$$Elongation = \sqrt{\frac{l}{w}},$$ (1)

is a measure of the largest length of the shape, l, versus the shortest width of the shape, w. An elongation value of 1 represents a perfect circle and an elongation value much less than one represents a stretched ellipse. Both circularity and compactness values were evaluated but did not show appreciable change and will not be discussed further.

18

A similar process to the one described above, was applied to the fringe region between the foam mat and the open water to determine the shape, size, and evolution of the foam patterns in the fringe region (Figure 6 box A). This method of analyzing the foam patterns in the fringe region was unsuccessful because the primary foam rings were filled with less dense foam that impacted the ability to determine a threshold value that appropriately classified foam from no foam regions. In order to determine the shape and size of these foam patterns, the cross-shore and along-shore diameter of the foam rings were calculated manually, and from these diameters, the areas and elongations of the foam rings were estimated.

The largest wave breaking events produced a small gap between the plunge point and the splash up due to bore collapse (Figure 6 box B). In this gap, small horizontal foam tubes developed in the cross-shore direction, connecting the plunge point and the location of the splash up due to bore collapse. To characterize the size and separation of these foam tubes, the gap region was selected and converted to a binary image. A line was selected in the along-shore direction that bisected these foam tubes. This bisecting line was then used to determine the width and spacing of the foam tubes as a function of time.

THIS PAGE INTENTIONALLY LEFT BLANK

III. RESULTS

An initial visual analysis of the video and still images was conducted to determine the general pattern of foam and foam hole distribution as the plunging wave broke and progressed toward the shore as a self-similar bore (Figure 6). There appears to be three distinct foam pattern regions within the wave breaking/run-up cycle. The first of these regions, henceforth called the gap region, occurs only during the largest plunging waves and is located between the plunge point and the location of the splash up due to bore collapse behind the wave front (Figure 6 box B). In this gap region there are several horizontal foam streaks oriented in the cross-shore direction that seem to connect the primary bore to the secondary splash point. This gap region exists for 1–4 seconds, depending on the height of the wave and the distance between the plunge point and the secondary splash. The next region of interest, hereafter called the fringe region, exists seaward of the wave immediately after the wave breaks (Figure 6 box A). A consistent line of boil like, foam rings, aligned in the along-shore direction mark the fringe region. These circular boils appear to grow slightly and become much more pronounced with elapsed time from wave breaking. The boils within the fringe region appear more elongated if the wave breaks closer to the shore or in a region still covered by the previous waves' foam mat. The third region is the primary foam region and it can be described as a dense mat of foam that appears directly behind the self similar bore just a few seconds after the wave breaks (Figure 6 boxes E and F). This mat of foam grows in extent as the bore progresses toward the shore. Several more seconds after the wave breaks the dense mat of foam begins to develop a visible pattern of nearly circular foam holes (Figure 6 circle D) starting first at the most seaward extent of the foam mat and extending toward the shore as the wave propagates. These foam holes appear to grow and become less circular (more elongated) with time elapsed since wave breaking and distance from wave crest.

21

Twenty-six bores are evaluated to quantitatively describe the evolution of the foam holes. The areas of the foam holes are calculated for each bore at each time step for the top sub-boxes. A mean area is then calculated for each of the twenty-six bores at each time step. These mean areas are then averaged to provide a time series of the ensemble mean area of all the bores (Figure 11a). The 95% confidence intervals and the linear regressions are also plotted. Each bore exists for a different length of time. Therefore, near the end of the time series there are fewer data points to average, causing the confidence interval to spread. The data are truncated past 16.33 seconds to account for this spread and the linear regression is only plotted for the first 10 seconds. This same process is repeated for the bottom sub-boxes (Figure 11b). For the top boxes the mean area of the foam holes is initially between 1 and 1.4 meters^2. For the first 4 seconds the area of the foam holes decreases linearly at a rate of 0.08 meters^2/second with a minimum mean area of approximately 0.9 meters^2 reached at t=4 seconds. After t=4 seconds the area of the foam holes increases linearly at a rate of 0.11 meters^2/second, reaching a maximum mean area of 2.3 meters^2 at t=15.6 seconds. For the bottom boxes the mean area of the foam holes at t=0 seconds is between 0.7 and 0.8 meters^2. The mean area increases linearly at a rate of 0.084 meters^2/second and reaches a maximum value of 1.86 meters^2 at t=9.3 seconds. The bottom boxes do not show the initial decrease in area that was seen in the top boxes because by the time the wave is in the bottom box region it is not a plunging breaker but rather a self-similar bore and there is no splash down cycle to cause the large foam holes.

Figure 11.   Area of Foam Holes All Bores (m^2) versus Time (sec)
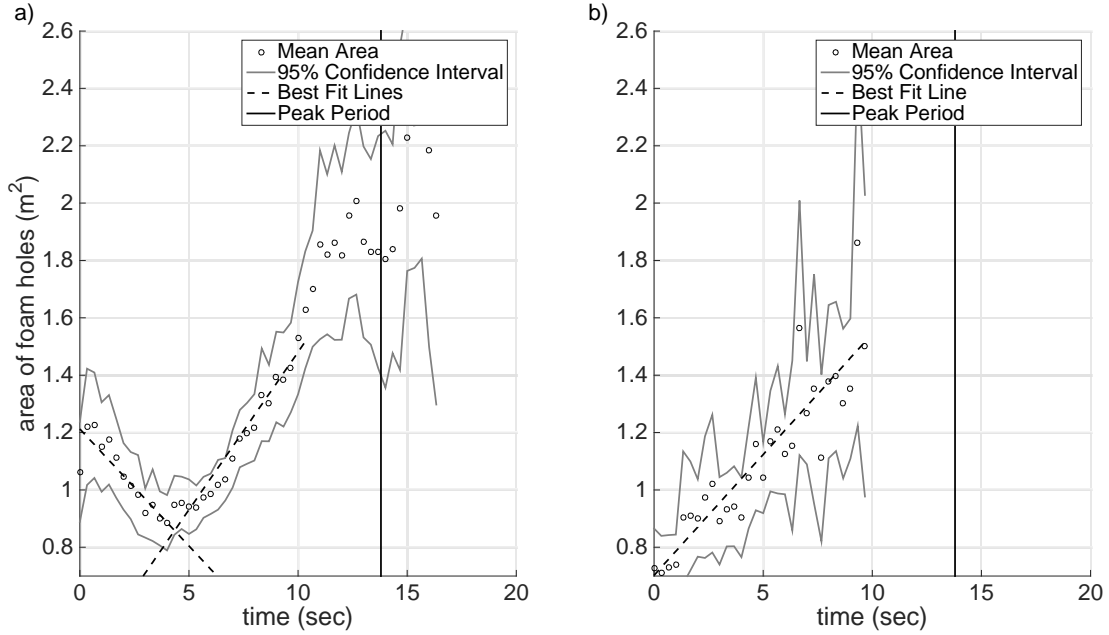
a) Top boxes. Slopes of best fit lines: -0.081 with an R^2 value of 0.78 and 0.11 with an R^2 value of 0.94. b) Bottom boxes. Slope of best fit line 0.084 with an R^2 value of 0.81. Gray line is 95% confidence interval, black dashed line is the best fit line, black vertical line is the peak wave period.

A similar process as was conducted above to calculate mean areas is used to calculate the mean elongation (Equation 1). A time series of these mean values is plotted to determine how the elongation of the foam holes changes with time (Figure 12). The elongation of the foam holes for the top boxes (Figure 12a) is initially 0.94 and decreases exponentially at a rate of 0.018/sec. The minimum elongation value at the end of the time series (excluding the final point) is 0.73 at t=16 seconds. The elongation of the foam holes for the bottom boxes at t=0 is 0.91 and decays exponentially at a rate of 0.021/sec. The minimum mean elongation of the foam holes in the bottom box is between 0.76 and 0.77 at t=9.6 seconds.

Figure 12.   Elongation of Foam Holes versus Time (sec)
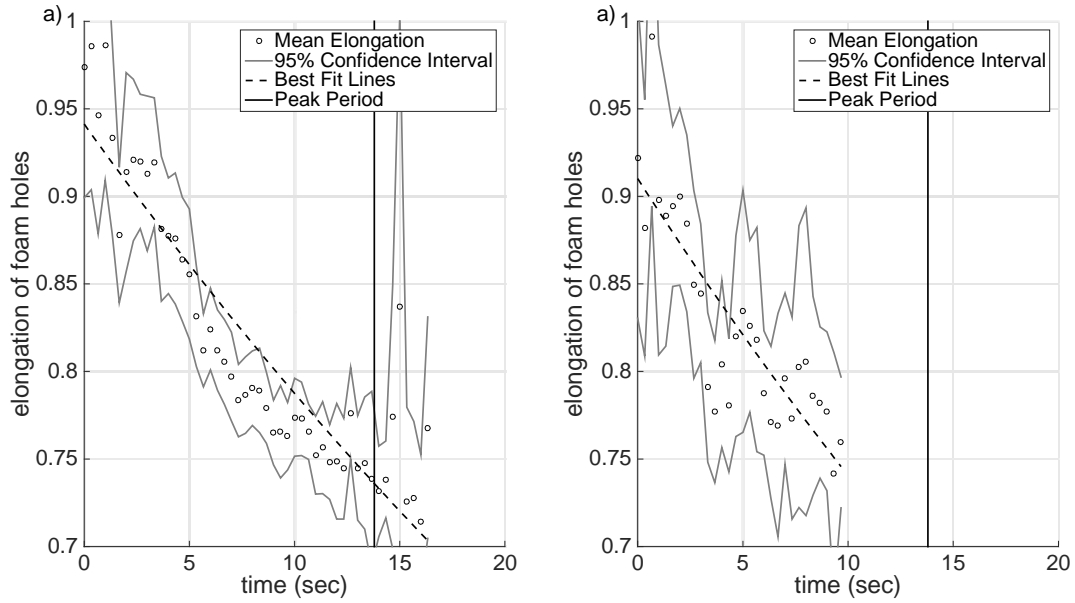
a) Top boxes. Exponential decay of best fit line -0.018/sec with an R^2 value of 0.83. b) Bottom boxes. Exponential decay of best fit line -0.021/sec with an R^2 value 0.72. Gray line is 95% confidence interval, black dashed line is the best fit line, black vertical line is the peak wave period.

While the time series of mean areas and mean elongations provide a general understanding of the foam hole evolution, they are not sufficient to describe the small details of the evolution of individual foam holes. A visual analysis of a small section of both top and bottom sub-boxes yields some interesting results that describe even more detail on how the foam holes evolve (Figures 13, 14 and 15). The areas of some of the foam holes grow by merging with other foam holes (Figure 15 red circles and pink ovals, Figure 13 pink ovals) while the area of certain other foam holes grow independent of their surroundings. Foam circles also appear to split apart (Figure 15 blue squares), thus decreasing in size. The elongation statistics discussed above show that the foam holes stretch but do not provide information on their axis of dilatation. By analyzing the small sub-boxes, it is apparent that the primary axis of dilatation is in the cross-shore direction (Figure 15 pink ovals, Figure 13 red circles and blue boxes, Figure 14 red circles). The statistics above do not describe how the foam holes move in reference to a fixed reference frame. By analyzing the small sub-boxes, it appears that the foam holes

24

translate slowly toward the shore (Figure 13 red circles and blue boxes, Figure 14 red circles). The foam holes appear to migrate faster in the bottom sub-boxes than they do in the top sub-boxes. There does not appear to be any rotation of the foam holes over time. The elongation of all the foam holes for one bore was plotted against the area of all the foam holes for the same bore. The elongation and area are not statistically correlated.

Figure 13.   Zoomed in Region of Bottom Boxes
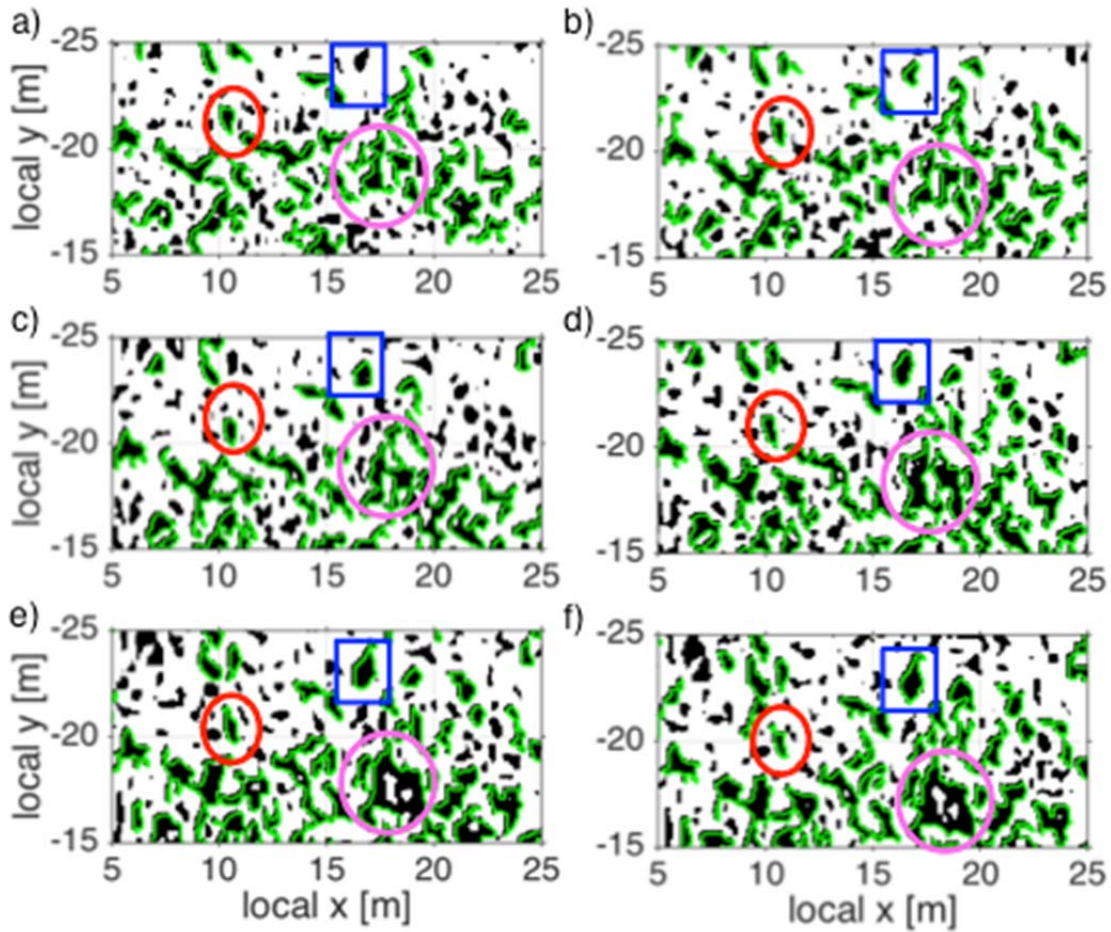
Time series of zoomed in region of bottom boxes for one bore starting at a) t = 4.33 seconds with time interval of .33 seconds. Red circled region depicts the elongation of a foam hole in the cross shore direction and the transport of the foam hole toward the shore. Blue squared regions show elongation and growth of foam holes in the cross shore direction as well as transport in the shoreward direction. Pink circled regions depict merging of foam holes and a small patch of remnant foam within a foam hole.

Figure 14.   Zoomed in Region of Bottom Boxes
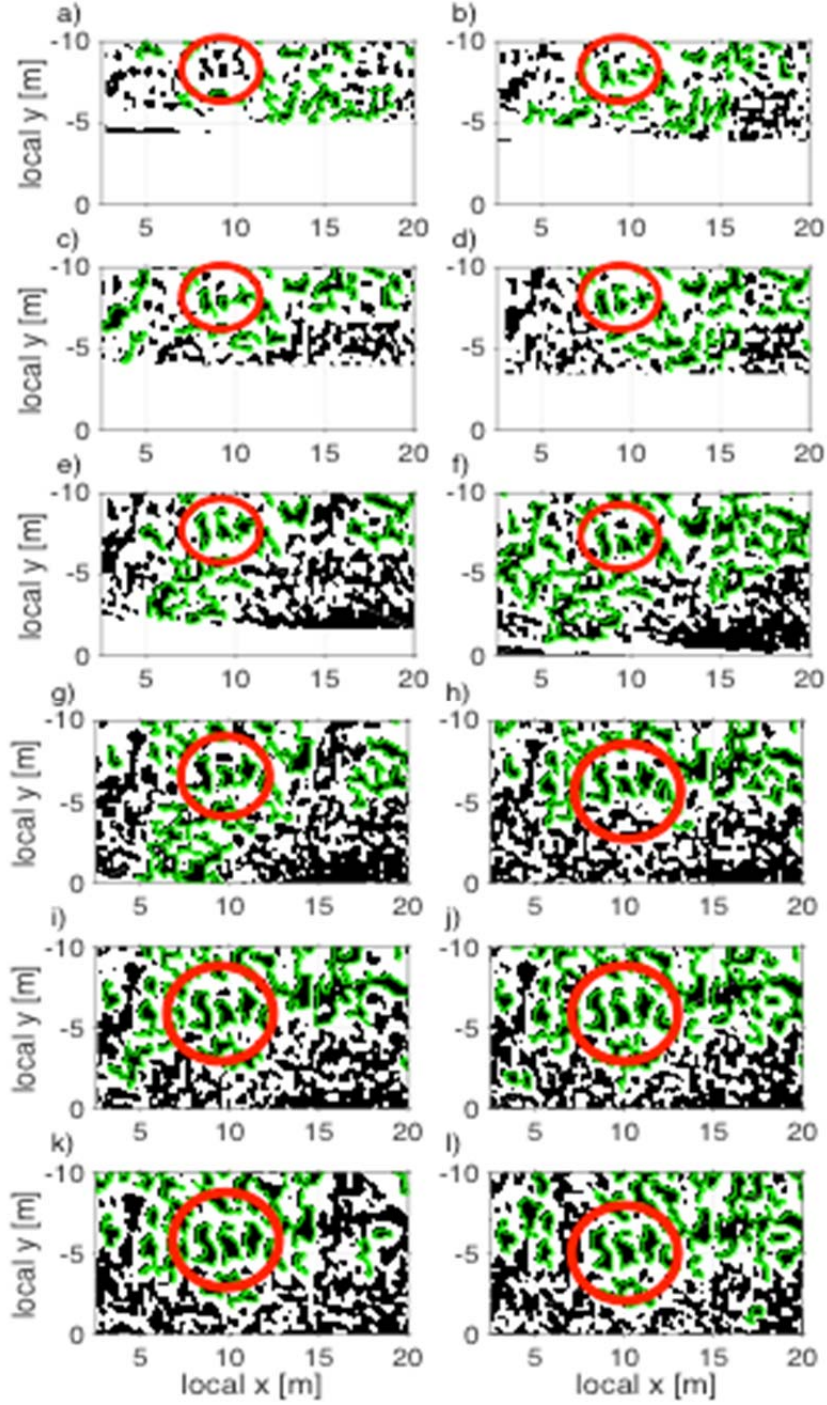
Time series of zoomed in region of bottom boxes for one bore starting at a) t = 6.66 seconds with time interval of .33 seconds. Red circled region depicts the elongation of a foam hole in the cross shore direction, the transport of the foam hole toward the shore and the growth of the foam hole.

Figure 15.   Zoomed in Region of Top Boxes
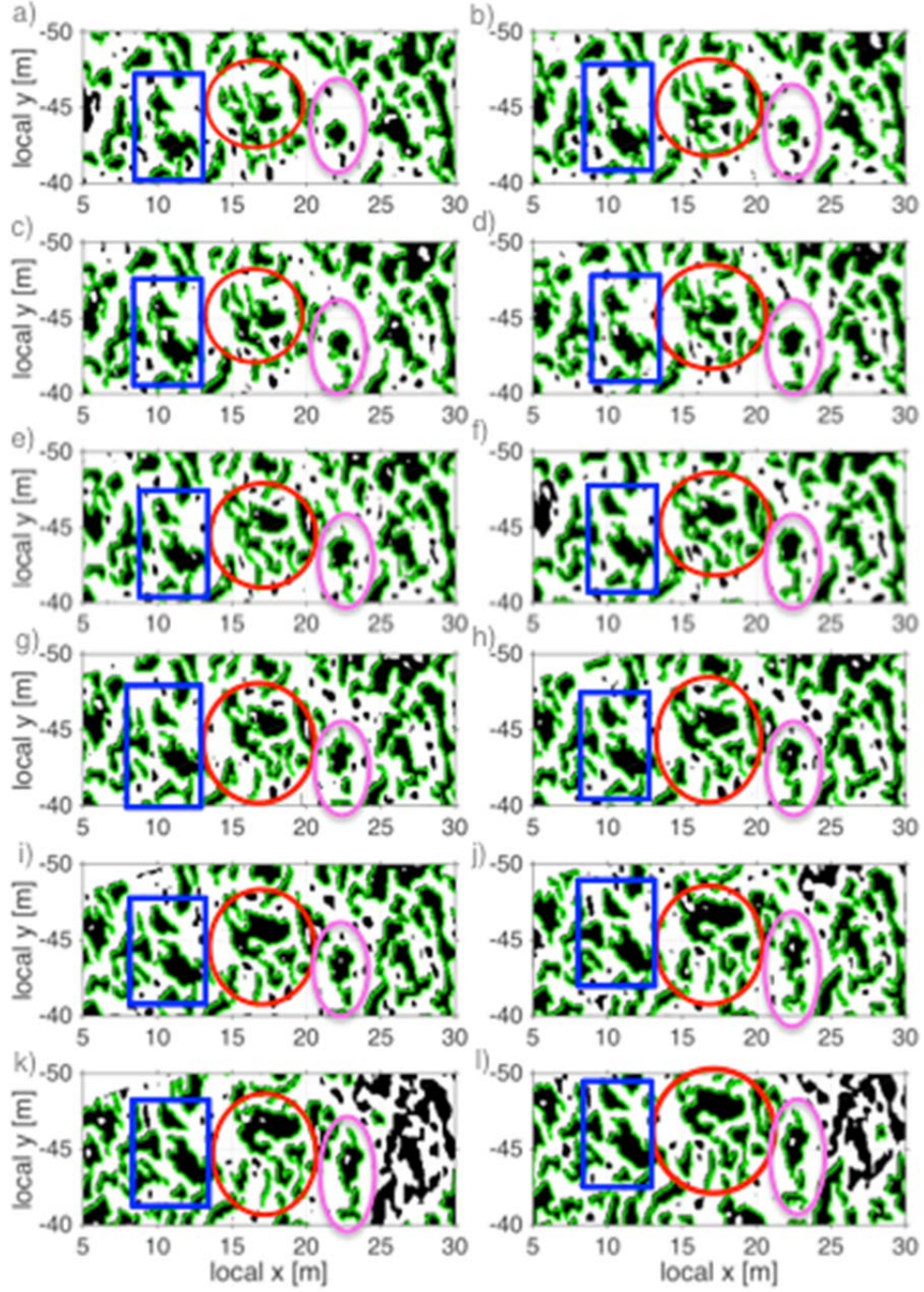

Time series of zoomed in region of top boxes for one bore starting at a) t = 10.66 seconds with time interval of .33 seconds. Red circled region depicts the growth of a foam hole by merging with other foam holes. Blue squared regions show foam holes splitting apart. Pink oval regions depict merging of foam holes and elongation in the cross-shore direction.

There were eight breaking waves that produced pronounced fringe regions (Figure 6 box A). The areas of five foam rings along the fringe region were calculated at each time step for each of these eight breaking waves. The mean area of the foam rings at each time step for each breaking wave was computed and then used to calculate a time series of the mean ensemble area of the foam rings for all eight of the breaking waves (Figure 16). The 95% confidence interval and linear regression were also calculated and are plotted along with the mean ensemble area. The mean area of the foam rings is initially 5 meters^2 and increases at a rate of 1.05 meters^2/second. After about 6 seconds the foam rings stop growing, maintaining a constant area of about 12 meters^2. Initially, the foam rings within the fringe region are filled with tiny bubbles. As time elapses, the center of the foam rings appear dark black, indicating there are no more bubbles present. The elongation of the foam rings was calculated but did not exhibit appreciable change.

Figure 16.   Area of Foam Rings in Fringe Region (m^2) versus Time (sec)
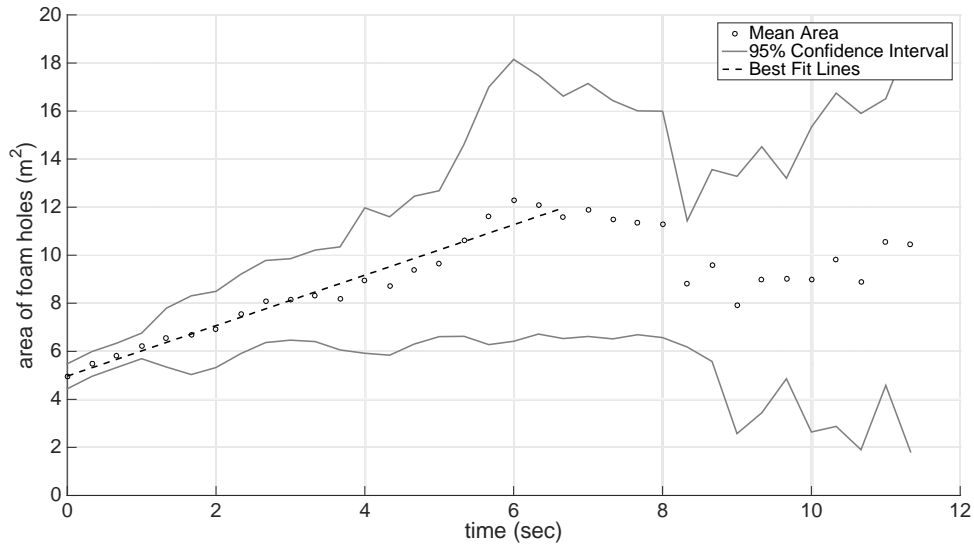
Slope of best fit line 1.05 meters^2/second with an R^2 value of .96. Gray line is 95% confidence interval, black dashed line is the best fit line.

The gap region between the plunge point and the secondary splash point is marked by horizontal foam tubes, oriented in the cross shore direction that seem to connect the plunge point to the secondary splash point (Figure 6 box B). Only one wave produced the conditions necessary to visualize the foam tubes for sufficient analysis. The width of these foam tubes was calculated and a time series of the average width of all the foam tubes at each time step was plotted. The foam tubes are only visible from the surface for approximately 3.5 seconds and they decrease in width with time. The initial width of the foam tubes is approximately 0.25 meters and decreases to a width of 0.1 meters.

THIS PAGE INTENTIONALLY LEFT BLANK

IV.   DISCUSSION

Thorpe et al. (1999) and Thorpe (2007) describe two physical processes that generate foam holes in the surf zone. The first of these processes are the ODEs/hairpin vortices that develop as a by-product of breaking waves. ODEs and hairpin vortices are observed in wave tanks as well as numerical modeling studies. Observing this phenomenon in the natural surf zone is difficult and to our knowledge no observations or measurements of ODEs/hairpin vortices have been made in the natural surf zone. The notion of using surface foam as a passive tracer to identify these features, and quantify their size and evolution is dependent on the ODE/hairpin vortex penetrating the ocean surface. Recent studies on ODEs/hairpin vortices have been focused on the layer between the free surface and above the bottom boundary layer (Ting 2006, Farahani and Dalrymple 2014, Ting and Reimnitz 2015) and do not consider the effects of the free surface on the ODE/hairpin vortex or the effect of the ODE/hairpin vortex on the free surface. Ting and Reimnitz (2015) reason that the ODEs/hairpin vortices must reach the free surface but what effect these features have on the transfer of mass at the surface is unknown.

Several studies on ODEs and hairpin vortices have been conducted using entrained bubbles as a flow visualization tool to describe and track the evolution of an ODE. These studies have been conducted in wave tanks, and the imagery has been acquired from the side to visualize the ODE as it extends down toward the bottom. Nadaoka et al. (1989) displayed a plan view photograph from one of their tank experiments and they assert that the "spotty features" in the image could be due to ODEs, but there are no data directly tying the surface foam spots to the presence of an ODE. Watanabe et al. (2005) describe the process of air entrainment in an ODE. They observed that bubbles with a certain amount of vorticity will be captured by the ODE and that these trapped bubbles will concentrate along the axis of rotation of the ODE, where the pressure is smallest. If the ODE does penetrate the surface, as Ting and Reimnitz (2015) claim, then the circular pattern on the surface, depicting the ODE, would be filled with bubbles and not free of bubbles as is evident in the collected imagery.

31

The measured area of the foam holes and the growth rate of the foam holes are incompatible with the hypothesis that ODEs/hairpin vortices create the discernable foam pattern on the surface is. The areas of the foam holes are between 0.8 and 2.0 meters^2 and the diameters are approximately 0.25 to 0.64 meters. The areas are also consistent between the top boxes, which are located farther offshore, and the bottom boxes, which are located closer to the beach. The size of ODEs/hairpin vortices is dependent on the depth of the water, where the width of the vortex is approximately ½ of the water depth (Ting and Reimnitz 2015). Video data herein shows that the area of the foam holes is independent of water depth, contrary to the concept of ODEs/hairpin vortices. Watanabe et al. (2015) observed through numerical modeling that the ODE elongates, and therefore, stretches over time owing to the conservation of angular momentum, the angular velocity increases and the radius of the ODE decreases. As described in chapter three of this paper, the foam holes consistently grow with time; therefore the foam holes within the dense mat of foam are not a passive tracer of an ODE/hairpin vortex in the water column below.

The second proposed method for foam hole generation is the theory of self-organization by rising bubbles. Bubbles of various sizes, and therefore buoyancies, are entrained into the water column during wave breaking. The larger bubbles rise faster than the smaller bubbles, imparting upward momentum on the surrounding liquid as they rise. When the large bubbles reach the surface they break and the momentum they imparted on their way to the surface spreads out laterally from the center of where the bubble burst. The smaller bubbles rise more slowly due to their lower buoyancy value. These small bubbles do not burst upon reaching the surface due to their size and surface tension. These bubbles are then spread out laterally from the center of their rise location by the momentum imparted by the large bubbles.

There are two pieces of evidence that do not support the theory of self-organization by rising bubbles. The first is the upward and outward momentum imparted by the large bubbles as they rise. Shortly after the large bubbles reach the surface the upward and then outward momentum will cease. The video evidence and statistical analysis of the foam holes shows that the foam holes continue to grow indefinitely and

not just for a few seconds as would be expected from the self-organization argument. The second piece of evidence that is incompatible with the self-organization by rising bubbles theory is the blackness of the foam holes immediately after formation. According to the self-organization by rising bubbles theory, there would be a stream of small bubbles rising after the large bubbles that would make the center of the foam hole appear gray or white for some time.

The theory of self-organization by rising bubbles could, however, describe the foam rings that develop in the fringe region (Figure 6 box A). These foam rings initially appear as bright rings of white foam with lighter, grayer foam in the center. This is consistent with the slow rise rate of the small bubbles into the center of the void that was produced by the bursting of the large bubbles. The center of the foam rings also become blacker and less gray with time elapsed since wave breaking, owing to the outward movement of the small bubbles. The rings grow for approximately 6 seconds and then remain a constant size, which corresponds with the outward momentum ceasing shortly after the large bubbles reach the surface.

The foam tubes that develop in the gap region of the largest plunging breakers are similar to the aerated vortex filaments that were predicted in the numerical simulation conducted by Lubin and Glockner (2015) and the surface scars simulated by Saruwatari et al. (2009). Much like the gap region foam tubes described in chapter three, the aerated vortex filaments modeled by Lubin and Glockner (2015) form between the plunge point and the splash-up location and are oriented in a cross-shore direction. These cross-shore, horizontal vortices develop in counter rotating pairs. In the upwelling region between a pair of vortices, the surface experiences divergent flow and in the downwelling region of a pair of vortices, the surface experiences convergent flow (Saruwatari et al. 2009). The surface foam formed by the breaking wave is concentrated along the region of convergence and downwelling. Because the foam bubbles are buoyant they remain at the surface and form distinct foam tubes in the cross-shore direction. In the upwelling region, bubble free water is brought to the surface and forms the bubble-free gaps between the foam tubes.

From the data collected in this experiment, there is still uncertainty as to the physical mechanisms that create and evolve the foam patterns in the surf zone. The next step in developing an understanding of these foam patterns is to conduct feature tracking on the images. In order to feature track the foam patterns, a stationary viewing platform is necessary. Feature tracking of the imagery discussed above was attempted, and although the georectification and georeferencing processes remove most of the wobble from the images, some remains, making the feature tracking process not possible. Another aspect that makes feature tracking of the foam patterns difficult is the changing nature of the foam. Unlike feature tracking a car or a face, the foam patterns are constantly changing and evolving; therefore, high-resolution stationary imagery is necessary. If feature tracking is successfully conducted, the surface macro-scale turbulence within the surf zone, which organizes the transport of foam at the surface, can be analyzed from a Lagrangian point of view. Lagrangian coherent structures (LCSs) are material lines that are advected by the flow (Peacock and Haller 2013). LCSs are classified as either attractors or repellers. In the region of these attractors and repellers, material develops into fillaments, similar to the foam patterns in the surf zone (Figure 17).

Figure 17.   Attracting and Repelling Lagrangian Coherent Structures
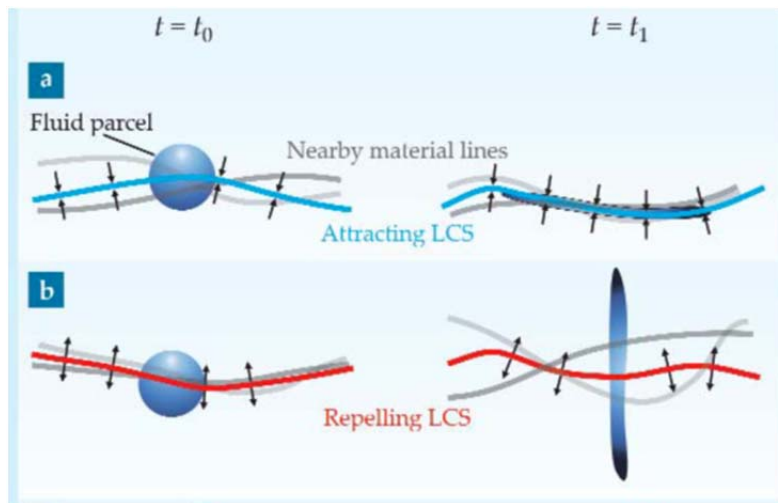
a) an attracting LCS b) a repelling LCS. Source: Peacock, T., and G. Haller, 2013: Lagrangian coherent structures: The hidden skeleton of fluid flows. *Phys. Today*, **66**, 41–47.

V.   CONCLUSION

Unique surf zone imagery, acquired from a UAV at Sand City, Monterey Bay, CA, is analyzed to describe the coherent foam patterns that evolve within the surf zone. On the day of collection, the narrow band waves were categorized as plunging, shore normal, breakers with a period of 13 seconds. Three distinct foam pattern regions are observed within the imagery (Figure 6). There is a dense mat of foam that develops into a coherent pattern of foam holes that grow and elongate with time. The fringe region exists on the seaward edge of the foam mat and is marked by rings of foam aligned in the along shore direction. These foam rings become more defined and larger with time. There is also a gap region that exists only during the largest plunging waves. The gap region forms between the plunge point and the secondary splash and is marked by foam tubes, aligned in the cross shore direction that appear to connect the plunge point to the secondary splash.

There are two hypotheses that describe the presence of the foam holes within the surf zone. The first hypothesis is that the ODEs/hairpin vortices created by the breaking waves cause the spotty foam appearance on the surface (Thorpe et al. 1999 and Thorpe 2007). The second hypothesis is that self-organization by rising bubbles causes foam holes within the surf zone (Thorpe et al. 1999 and Thorpe 2007). By analyzing the UAV imagery of the surf zone, both of these theories are tested.

The first step to analyzing the video imagery is to convert the video to still images. Then, the still images are georectified and georeferenced so that the size of the features within the surf zone can be measured. The color images are then converted to binary images, using an interactive selection technique (Grande 2000), so that the foam holes can be distinguished from the foam. The foam mat region is split into two sub-boxes based on the size of the foam holes (Figure 7). Twenty-six individual bores are analyzed and the area and elongation statistics of the foam holes in each box are calculated. The mean area and elongation are calculated for each bore and each box, and then a time series of the ensemble mean area and elongation is plotted for all the bores, for each box. Also plotted are the linear regression and the 95% confidence interval.

35

The mean area of the foam holes for the top box decrease for the first 4 seconds and then increases at a rate of 0.11 meters^2/second. The mean area of these foam holes range from 0.9 meters^2 to 2.3 meters^2. The mean area of the foam holes for the bottom box range from .7 meters^2 to 1.86 meters^2. The mean area of the foam holes for the bottom box increases linearly at a rate of 0.084 meters^2/second. The mean elongation of the foam holes for both the top and bottom box was found to decrease, becoming more elongated with time. For both the top and bottom box, the elongation values were initially 1.0 and decreased linearly at a rate of 0.014 for the top box, and 0.017 for the bottom box. The final elongation value for both the top and bottom box were between 0.7 and 0.75. Based on these statistical results and visual analysis of the video data, both hypotheses for foam hole generation within the surf zone are incompatible with results. The next step in quantitatively describing the foam patterns within the surf zone is to conduct feature tracking, which requires a stationary viewing platform. Once feature tracking is conducted, the surf zone foam patterns can be viewed from a Lagrangian perspective. The LCSs can be calculated to provide information on the material lines that concentrate and advect flow, leading to an understanding of the macro-scale turbulence within the surf zone.

The mean area and elongation of the foam rings along the fringe region were analyzed, and the rings grow at a rate of 1.05 meters^2/second. The foam rings do not elongate with time. From a visual analysis, the foam rings are initially filled with small bubbles, but as time progresses the center of the foam rings appear black indicating all bubbles have disappeared. It is reasonable to assume that the generation of foam rings within the fringe region is caused by the self-organization due to bubble rise and not the presence of ODEs/hairpin vortices.

Within the gap region, the width of the foam tubes, and the spacing between the foam tubes were analyzed. Only one wave produced conditions conducive to foam tube generation. These foam tubes are only visible from the surface for a few seconds and decrease in width over time. These foam tubes are not likely caused by the ODE/hairpin vortex theory or self-organization due to bubble rise, but are rather created by the convergent regions between a pair of counter rotating vortices, while the gaps between

the foam tubes likely indicate the divergent regions between a pair of counter rotating vortices (Saruwatari et al. 2009 and Lubin and Glockner 2015).

THIS PAGE INTENTIONALLY LEFT BLANK

LIST OF REFERENCES

Battjes, J. A., 1974: Surf similarity. *Coastal Engineering Proceedings*, 466–480.

Brouwer, R. L., M. A. de Schipper, P. F. Rynne, F. J. Graham, A. J. H. M. Reniers, and J. H. MacMahan, 2015: Surfzone monitoring using rotary wing unmanned aerial vehicles. *J. Atmos. Ocean. Technol.*, **32**, 855–863, doi:10.1175/JTECH-D-14-00122.1.

Carini, R. J., C. C. Chickadel, A. T. Jessup, and J. Thompson, 2015: Estimating wave energy dissipation in the surf zone using thermal infrared imagery. *J. Geophys. Res. Ocean.*, **120**, 3937–3957, doi:10.1002/2014JC010561.Received.

Derakhti, M., and J. T. Kirby, 2014: Bubble entrainment and liquid–bubble interaction under unsteady breaking waves. *J. Fluid Mech.*, **761**, 464–506, doi:10.1017/jfm.2014.637.

DJI, 2015: DJI Phantom 2 Vision+. Accessed October 8, 2015. [Available online at http://www.dji.com/product/phantom-2-vision-plus/feature.]

FAA, 2015: Press Release – DOT and FAA Propose New Rules for Small Unmanned Aircraft Systems. Accessed November 23, 2015. [Available online at http://www.faa.gov/news/press_releases/news_story.cfm?newsId=18295.]

Farahani, R. J., and R. a. Dalrymple, 2014: Three-dimensional reversed horseshoe vortex structures under broken solitary waves. *Coast. Eng.*, **91**, 261–279, doi:10.1016/j.coastaleng.2014.06.006.

Grande, J. C., 2000: Principles of Image Analysis. *Practical Guide to Image Analysis*, E.J. Kubel, Ed., A S M International, 75–100.

Heikkila, J., and O. Silven, 1997: A four-step camera calibration procedure with implicit image correction. *Proceedings of IEEE Computer Society Conference on Computer Vision and Pattern Recognition*, 1106–1112. [Available online at http://ieeexplore.ieee.org/lpdocs/epic03/wrapper.htm?arnumber=609468.]

Komar, P. D., 1998: *Beach Processes and Sedimentation*. 2nd ed. Prentice Hall, 544 pp.

Longuet-Higgins, M. S., and J. S. Turner, 1974: An "entraining plume" model of a spilling breaker. *J. Fluid Mech.*, **63**, 1–20, doi:10.1017/S002211207400098X.

Lubin, P., and S. Glockner, 2015: Numerical simulations of three-dimensional plunging breaking waves: generation and evolution of aerated vortex filaments. *J. Fluid Mech.*, **767**, 364–393, doi:10.1017/jfm.2015.62.

MacMahan, J. H., E. B. Thornton, T. P. Stanton, and A. J. H. M. Reniers, 2005: RIPEX: Observations of a rip current system. *Mar. Geol.*, **218**, 113–134, doi:10.1016/j.margeo.2005.03.019.

Nadaoka, K., and K. T., 1982: Laboratory measurements of velocity field structure in the surf zone. *Coast. Eng. J.*, **25**, 125–145.

Nadaoka, K., M. Hino, and Y. Koyano, 1989: Structure of the turbulent flow field under breaking waves in the surf zone. *J. Fluid Mech.*, **204**, 359–387.

Peacock, T., and G. Haller, 2013: Lagrangian coherent structures: The hidden skeleton of fluid flows. *Phys. Today*, **66**, 41–47.

Peregrine, D. H., 1983: Breaking Waves On Beaches. *Annu. Rev. Fluid Mech.*, **15**, 149–178.

Podobna, Y., J. Schoonmaker, J. Dirbas, J. Sofianos, C. Boucher, and G. Gilbert, 2010: Multi Channel Imager for Littoral Zone Characterization. *SPIE*, Vol. 7664 of, 1–12. [Available online at http://proceedings.spiedigitallibrary.org.libproxy.nps.edu/proceeding.aspx?articlei d=762449.]

Rogers, B. D., and R. A. Dalrymple, 2004: SPH modeling of breaking waves. *Coastal Engineering*, 415–427.

Saruwatari, A., Y. Watanabe, and D. M. Ingram, 2009: Scarifying and fingering surfaces of plunging jets. *Coast. Eng.*, **56**, 1109–1122, doi:10.1016/j.coastaleng.2009.08.007.

Thornton, E. B., 1979: Energetics of breaking waves within the surf zone. *J. Geophys. Res.*, **84**, 4931, doi:10.1029/JC084iC08p04931.

Thorpe, S. A., 2007: *An introduction to ocean turbulence*. Cambridge University Press, 240 pp.

Thorpe, S. A., W. A. M. Nimmo Smith, A. M. Thurnherr, and N. J. Walters, 1999: Patterns in foam. *Weather*, **54**, 327–334.

Ting, F. C. K., and J. Reimnitz, 2015: Volumetric velocity measurements of turbulent coherent structures induced by plunging regular waves. *Coast. Eng.*, **104**, 93–112, doi:10.1016/j.coastaleng.2015.07.002.

Turner, J. S., and I. L. Turner, 2011: Foam patches behind spilling breakers. *J. Mar. Res.*, **69**, 843–859, doi:10.1357/002224011799849336.

Watanabe, Y., H. Saeki, and R. J. Hosking, 2005: Three-dimensional vortex structures under breaking waves. *J. Fluid Mech.*, **545**, 291–328, doi:10.1017/S0022112005006774.

Wojnar, L., and K. J. Kurzydlowski, 2000: Analysis and Interpretation. *Practical Guide to Image Analysis*, E.J. Kubel, Ed., ASM International, 145–202.

Zhang, Z., 2000: A flexible new technique for camera calibration. *IEEE Trans. Pattern Anal. Mach. Intell.*, **22**, 1330–1334, doi:10.1109/34.888718.

THIS PAGE INTENTIONALLY LEFT BLANK

INITIAL DISTRIBUTION LIST

1.   Defense Technical Information Center
     Ft. Belvoir, Virginia

2.   Dudley Knox Library
     Naval Postgraduate School
     Monterey, California